Taking topological insulators for a spin

de Vries, Eric Kornelis

Chapter 2

Properties of topological insulators

In this chapter, I will discuss the origin of the novel properties of topological insulators that is based on topological band theory — the basis for understanding topological insulators and topological superconductors. In the first section, the crystal structure of the topological insulators used in this thesis will be discussed which is needed for considerations in subsequent sections. After having identified the type of elements and the symmetries in these crystals, an introduction to topological band theory will be given through simple models of the quantum Hall effect, the Haldane model for graphene, and the extension of the Haldane model by Kane and Mele. This picture will then be extended to two-dimensional topological states in HgTe quantum wells and three-dimensional Bi-based topological insulators where the Bi-based compounds are of our main interest. Furthermore, I will look into the types of growth of these materials. Additional theoretical concepts supporting the experiments will be treated in every following chapter.

2.1 Crystal structure

The group of topological insulators that is studied in this thesis belongs to the class of (V)–(VI)-semiconductors where (V)-elements Sb and Bi and (VI)-elements Se and Te are considered with a stoichiometry $(V)_2(VI)_3$. This family of compounds is arranged in a rhombohedral crystal structure with space group $R\bar{3}m$ (D_{3d}^5 in Schönflies notation) that is spanned by the translational vectors $\boldsymbol{a}_i$ (see figure 2.1):

$$\boldsymbol{a}_1 = \left(\frac{-a}{2}, \frac{\sqrt{3}a}{6}, \frac{c}{3}\right), \boldsymbol{a}_2 = \left(\frac{a}{2}, \frac{-\sqrt{3}a}{6}, \frac{c}{3}\right), \boldsymbol{a}_3 = \left(0, \frac{\sqrt{3}a}{3}, \frac{c}{3}\right), \quad (2.1)$$

where a and c are given in table 2.1. From the relation $\boldsymbol{a}_i \cdot \boldsymbol{b}_j = 2\pi\delta_{ij}$ between real and reciprocal vectors the following reciprocal vectors $\boldsymbol{b}_j$ are obtained:

$$\boldsymbol{b}_1 = \frac{2\pi}{a}\left(-1, \frac{-\sqrt{3}}{3}, \frac{a}{c}\right), \boldsymbol{b}_2 = \frac{2\pi}{a}\left(1, \frac{-\sqrt{3}}{3}, \frac{c}{a}\right), \boldsymbol{b}_3 = \frac{2\pi}{a}\left(0, \frac{2\sqrt{3}}{3}, \frac{a}{c}\right). \quad (2.2)$$

The unit cell of the crystal structure consists of 15 atomic layers where a basic unit of five atomic layers, termed as a quintuple layer with a height of roughly 1 nm, is stacked according to $(VI)^B\text{-}(V)^C\text{-}(VI)^A\text{-}(V)^B\text{-}(VI)^C$ where A, B, and C correspond to the lattice sites that the atoms can occupy (see figure 2.1). It is important to realize that a quintuple layer is always (VI)-terminated and therefore the interlayer spacing is larger than the intralayer spacing, which gives rise to Van der Waals bonding between the quintuple layers and covalent bonding within a quintuple layer. Due to the relatively weak Van der Waals bonding it is therefore possible to mechanically cleave such materials at the Van der Waals gap, yielding pristine interfaces for investigation (see section 2.4.2).

The supercell lattice with space group $R\bar{3}m$ has three symmetry operations, namely inversion i, three-fold rotation c_{3z}, and reflection σ_x. The presence of inversion symmetry in this crystal is important for a simplified determination of the topological invariant as discussed in section 2.2. However, it is important to realize that the inversion symmetry is broken at the (VI)-terminated surface which yields the reduced symmetric group C_{3v}^5 and is important for surface sensitivity in optical experiments (see chapter 4).

Compound	a (Å)	c (Å)
Sb_2Te_3	4.250	30.35
Bi_2Te_3	4.383	30.49
Bi_2Se_3	4.138	28.64
Sb_2Se_3	4.076	29.83

Table 2.1: Overview of the lattice constants a and c for the discussed $(V)_2(VI)_3$ compounds [1, 2]. It has been observed for Sb_2Te_3 and Bi_2Se_3 that the lattice constants a and c change between 0.2 and 0.4% with temperatures changing from 10 to 270 K [3].
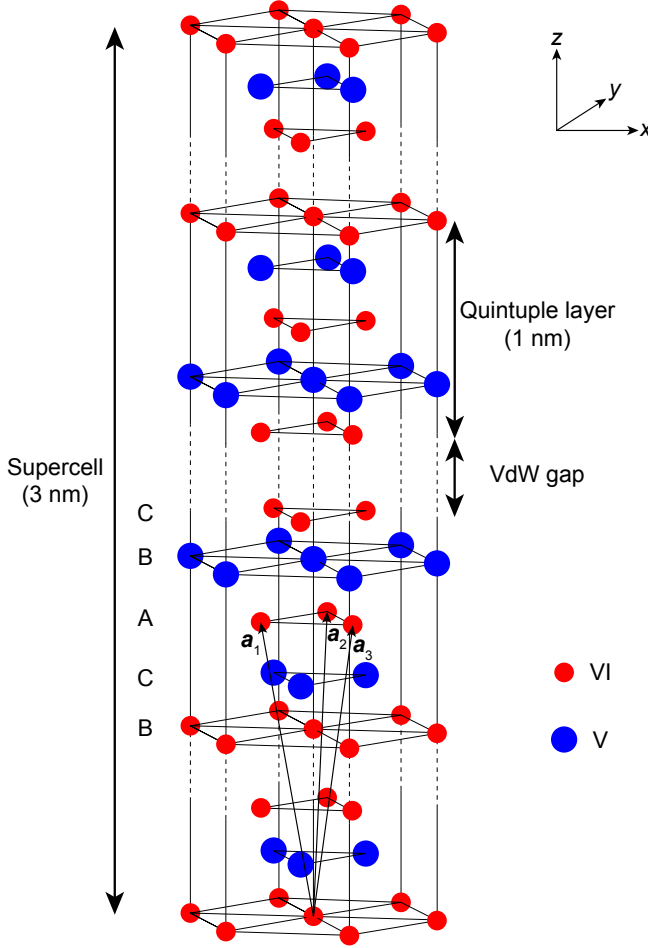
Figure 2.1: Crystal structure of the studied $(V)_2(VI)_3$ family of compounds. The structure consists of (V)-atoms (blue) and (VI)-atoms (red) located in A, B, and C planes within a supercell of 15 atomic layers ($\sim$3 nm) with inverted-repeating quintuple layer basic units ($\sim$1 nm) that are separated by a Van der Waals gap (VdW gap), as indicated by the dashed lines. The crystal is spanned by translational vectors $\boldsymbol{a}_i$. Figure inspired by [1].

2.2   Topological band theory

In this section, I provide a treatment along the lines of a very instructive paper by Hasan and Kane [4] with additional insights from online course material provided by the Technical University of Delft [5]. I have tried to introduce the most important physical concepts for the reader without going into lengthy mathematical details.

Topological band theory studies similarities between gapped electronic band structures of different systems based on the topology of the occupied bands. These simi-

larities are characterized by integer topological invariants, the applicability of which depends on the symmetries of the system. By their topological invariants, insulators (including vacuum) are for example termed as topologically trivial whereas systems with a different topology as topologically nontrivial. Differences in topological character yield interesting phenomena at the interface of such combined systems.

The first example of such a nontrivial system is the quantum Hall state where the Hall conductivity of a two-dimensional (2D) electron gas is quantized in integer steps of e^2/h under an applied magnetic field [6], see figure 2.2a. In a quantum-mechanical picture, the bands are Landau quantized and further Zeeman split under large magnetic fields with the Fermi level located in between two of such Landau levels [figure 2.2b, case (i)]. In the bulk, there are no states at the Fermi level such that transport is impossible. Classically, the electron's orbit can be completed and the electrons get localized. However, at the edges a local potential is present (otherwise the electrons are not confined to the material slab) that bends up the bands that cross the Fermi level. This leads to edge state transport with a linear dispersion close the Fermi level [7]. Such edge states can be visualized as skipping orbits with an opposite group velocity at both edges of the sample, which can be seen from the opposite slopes at the edges in figure 2.2b. It is important to realize that these edge states do not have any states to backscatter to and thus are channels with each a maximum possible conductivity bound by quantum mechanics, e^2/h per channel[1]. Since charge transport only occurs via these 'chiral' edge states, the longitudinal conductivity is zero, i.e. the same number of electrons reach both probe contacts yielding a zero potential difference. However, due to the applied potential difference the number of electrons leaving each source contact is different and therefore the edge states carry a different number of electrons. This leads to a measurable Hall conductivity that is dependent on the number of edge states crossing the Fermi level. By now varying the magnetic field, the Landau-level spacing can be changed, leading to a change in the number of involved edge states. Upon crossing a Landau level at the Fermi energy [figure 2.2b, case (ii)], the bulk participates in the transport and a longitudinal resistance can be measured shortly and then vanishes again.

As already can be seen from this 'classical' picture, it is expected that the Hall conductivity is quantized because it depends on the integer number of edge states that are crossed by the Fermi level. This quantization is rooted in the topology of the quantum Hall state that can be characterized by the Chern number, as realized by Thouless et al. [8]. The Chern number can be evaluated from the Berry phase [9], which is a geometrical phase factor that is obtained by a quantum-mechanical state under cyclic adiabatic evolution of a state, i.e. the phase that is picked up while traversing a closed loop through momentum space. The acquired Berry phase $\gamma_n(C)$ for the nth state over a closed path C that defines a surface $\boldsymbol{S}$ can be calculated by taking the surface integral over the Berry curvature $\boldsymbol{V}_n$:

$$\gamma_n(C) = -\iint_C \mathrm{d}\boldsymbol{S} \cdot \boldsymbol{V}_n(\boldsymbol{R}) = -\iint_C \mathrm{d}\boldsymbol{S} \cdot [\nabla_{\boldsymbol{R}} \times \boldsymbol{A}(\boldsymbol{R})], \qquad (2.3)$$

---

[1]In contrast to quantum point contact measurements, where $2e^2/h$ per channel is measured due to spin degeneracy, the Landau levels are spin split by the Zeeman interaction and thus leading to e^2/h per channel.
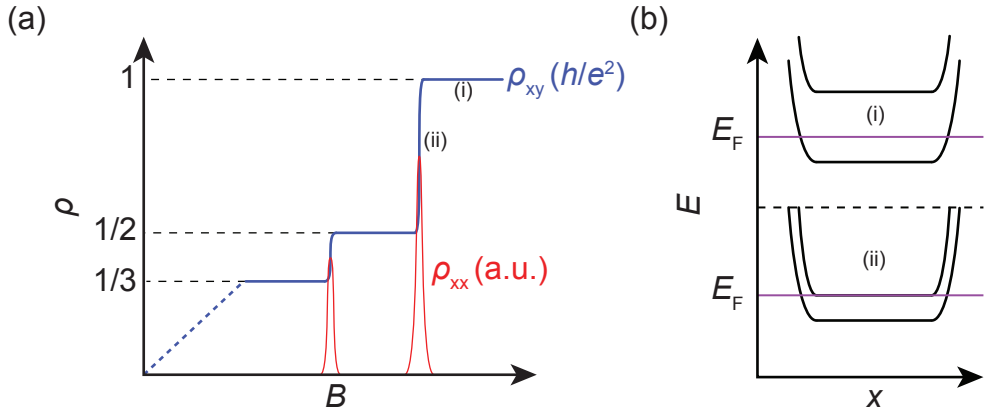
Figure 2.2: (a) Schematics of magnetic-field-dependence of Hall resistivity ρ_{xy} (units of h/e^2) and longitudinal resistivity ρ_{xx} [arbitrary units (a.u.)]. (b) Landau level spectrum over a quantum Hall state slab defined in the x direction for cases (i) and (ii) as depicted in (a).

where $\boldsymbol{R}$ is the parameter to describe the path C, and $\boldsymbol{A}$ is the Berry potential (or Berry connection). The integer Chern invariant is then obtained by integrating over the full Brillouin zone in momentum space [8]. Summing these invariants over all occupied bands will yield the total Chern number n_C that is locked to the particular band structure, i.e. this number cannot be changed by smoothly varying the Hamiltonian unless the band gap is closed. For the quantum Hall state, the Chern number is nonzero and therefore this system is topologically different from its environment (say vacuum). The difference in Chern number requires a crossover state at the edge. In this case, the state can be depicted as the potential difference at the edges between the bulk Landau levels and the vacuum's conduction band[2]. Notably, a bulk is needed that accommodates states at *both* edges, since a single edge state would yield loss of charge, which is compensated for by the other edge state via the bulk.

The quantum Hall state requires a magnetic field to break time-reversal symmetry [$\hat{H}(\boldsymbol{k}) = \hat{H}(-\boldsymbol{k})$, with $\hat{H}$ the Hamiltonian], but there are other systems where time-reversal symmetry can be broken without application of a magnetic field. An example of such a system has been hypothesized by Haldane [10] where graphene is subject to a magnetic field that is zero on average[3] and complex next-nearest-neighbor hopping is present, which together break time-reversal symmetry in the system. The breaking of this symmetry introduces a mass term that leads to opening of a band gap with a negative mass (inverted bands) at one of the high symmetry points $\boldsymbol{K}$ and $\boldsymbol{K'}$ due to preservation of inversion symmetry [$\hat{H}(\boldsymbol{k}) = -\hat{H}(-\boldsymbol{k})$]. At the interface with a trivial system that does not have an inverted mass at one of those points, a crossover state is

---

[2]One can visualize this as the lowest occupied bulk Landau level, which normally has a conduction-band character, now looks like the maximum of the valence band.

[3]Haldane imagined to generate such a magnetic field by introducing a ferromagnetic atom inside every hexagonal unit cell. The net flux is zero because fields from neighboring cells cancel out the fields of the atom in the actual unit cell. A similar approach has been used to realize the quantum anomalous Hall effect in topological insulators [11,12] where an inverted band gap is opened at one of the surfaces by adding a mass term through magnetic doping.

required that is very similar to the chiral edge state as observed for the quantum Hall state. The existence of such a state can again be related to integration of the Berry phase over the Brillouin zone. Both Dirac points in the Brillouin zone contribute a Chern number of $\frac{1}{2}$ and depending on whether the masses are equal or opposite to each other, a Chern number of 0 or 1 will be obtained. This edge state (or Chern number) cannot be removed (turn zero) unless the band gap is closed in order to obtain equal masses or noninverted bands at the $\boldsymbol{K}$ and $\boldsymbol{K'}$ points and therefore these edge states are topologically protected. In the same toy model, Haldane has further discussed that a 'zero-energy' Landau level that is half filled at each $\boldsymbol{K}$ and $\boldsymbol{K'}$ is present when the system is subject to a magnetic field, such that a Hall conductivity of e^2/h is obtained again (similar to the shared contribution to the Chern number of every Dirac point in the Brillouin zone). Such Landau levels are characteristic for Dirac surface states with linear dispersion, such as present in graphene and three-dimensional (3D) topological insulators. Furthermore, these Landau levels change the filling-factor labeling for Shubnikov–de Haas oscillations with respect to trivial systems, as will be discussed shortly in chapter 5.

For generation of the quantum Hall state in Haldane's model a complex next-nearest-neighbor hopping term has to be included to break time-reversal symmetry in the material, but there is an intrinsic effect that can cause a similar nontrivial state while preserving the symmetry. In 2005, Kane and Mele investigated the effect of spin–orbit coupling in graphene (expanding the work of Haldane) that was ignored before because of its relatively small size [13]. Instead of a gap opening by breaking time-reversal symmetry, spin–orbit coupling yields a finite energy gap with again opposite masses at the $\boldsymbol{K}$ and $\boldsymbol{K'}$ points. As a result of including the spin degree of freedom, a quantum spin Hall state is observed where a spin-filtered (spin current $\boldsymbol{J_s} \neq 0$), counterpropagating (charge current $\boldsymbol{J_c} = 0$) edge-state pair is present (see figure 2.4a). Taking both edges into account a two-terminal conductance of $2e^2/h$ is expected, whereas the Hall conductivity is zero now since there are counterpropagating states at each edge. Due to the spin texture of these one-dimensional (1D) states that is present due to the conservation of time-reversal symmetry, elastic backscattering is not allowed since it would have to include a spin flip. The importance of spin–orbit coupling for topological distinction requires expansion of the topological invariants since the Chern number n_{C} is zero in a time-reversal invariant system. Therefore, the new topological invariant ν_0 was introduced for this new class of 'Z_2 topological insulators' [14][4].

Upon conservation of time-reversal symmetry, Bloch Hamiltonians should be time-reversal invariant and this poses an important constraint for band structures which is known as Kramers' theorem. The theorem tells that the eigenstates of the Hamiltonian must be degenerate at the time-reversal-invariant momenta $k = 0, \pi/a$. Away from these special points, spin–orbit coupling lifts this degeneracy as in the case of graphene including spin–orbit coupling. Now, there are two configurations in which the crossover (edge) states between the time-reversal-invariant momentum points in such a system can connect (see figure 2.3): in the first case the same pair of states

---

[4]In three dimensions, a time-reversal invariant band structure is actually characterized by four Z_2 invariants ν_0, ν_1, ν_2, and ν_3 where the latter three are not robust against disorder and classify weak topological insulators [15,16].
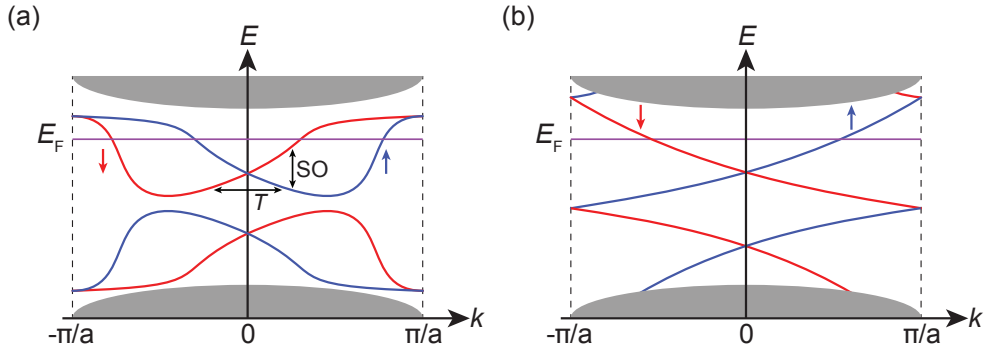
Figure 2.3: Dispersion of spin-textured edge states (blue and red colors indicate spin species) with (a) topologically trivial and (b) topologically nontrivial character. The gray bands indicate the bulk bands and E_F the Fermi level. As depicted in (a), the spin–orbit coupling (SO) gives rise to the spin splitting of the bands, whereas the time-reversal symmetry T forms pairs located at k and $-k$.

are shared between the time-reversal-invariant points whereas for the second case the pairs are 'split'. For the first case, the states can be pushed out of the band gap by tuning the Hamiltonian smoothly and therefore will yield $\nu_0 = 0$. In the second case, it is not possible to remove the states completely out of the band gap without closing it, i.e. there will always be a pair of states crossing the Fermi level, and therefore $\nu_0 = 1$. The odd number of crossing pairs with the Fermi level E_F compared to an even number of crossing pairs in the first case, is secured and gives rise again to topological protection of these edge states[5]. The number of crossing pairs gives rise to $\nu_0 = 1$. The calculation of ν_0 can be performed in various ways of which an overview has been given in [4]; one of them is integrating the phase of the Pfaffian over the Brillouin zone [14]. Such a calculation shows similarities with that of the Chern number, integrating the Berry phase, as introduced earlier.

Since graphene is a light-element material, the gap opening due to spin–orbit coupling is calculated to be rather small and the quantum spin Hall state will therefore be difficult to detect experimentally [18, 19]. Therefore, it is logical to investigate materials with a much stronger spin–orbit coupling. In 2006, Bernevig, Hughes, and Zhang proposed such a 2D topologically nontrivial system in a HgTe quantum well beyond a certain critical thickness of the HgTe layer [20]. Around this critical thickness the bands closest to the Fermi level exchange position, changing the total parity of the system (see below for a more detailed discussion on the classification by parity). Experimental evidence of a quantized conductance that can be related to the topologically protected edge states (as in figure 2.4a) followed a year later [21]. The mobility of the charge carriers in the quantum wells turned out to play a decisive

---

[5]One can visualize this protection when the material is connected to a trivial substrate (or vacuum). This trivial substrate can only push out an even number of states crossing the Fermi energy such that for the topologically nontrivial case not all the states can be removed [17].
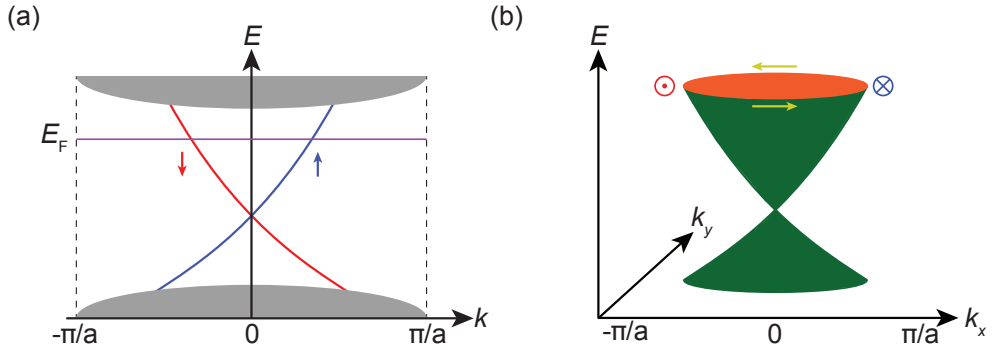
Figure 2.4: (a) Schematic depiction of the topological, spin-textured 1D edge state dispersion in 2D systems such as the Kane–Mele graphene model and HgTe quantum wells. (b) Topological, spin-textured 2D surface state dispersion for 3D systems. The dispersions are shown only for a single material boundary.

role[6]. Later on, the nonlocal character of the edge states and the spin-filtering of those states were reported [22, 23], making this quantum spin Hall insulator suitable for spintronic applications.

The picture in two dimensions can be extended to a 3D picture where surface states exist that must be Kramers degenerate at the four time-reversal invariant momentum points in the surface Brillouin zone. At any other momentum point the degeneracy is lifted again by the spin–orbit coupling. In the case of strong 3D topological insulators ($\nu_0 = 1$) an odd number of Dirac points are enclosed by the surface Fermi circle and this gives rise to the topological protection. Due to the time-reversal symmetry in these materials opposite spins are present at momenta k and $-k$ and this leads to a spin orientation s rotating along the circle (see figure 2.4b). It is important to remember how spin–orbit coupling and time-reversal symmetry change the band structure picture of the surface states. Spin–orbit coupling leads to spin splitting away from the time-reversal-invariant momentum points in half of the Brillouin zone ($+k$) and time-reversal symmetry copies these split states to the other half of the Brillouin zone while inverting the spin (reflecting states at $+k$ onto $-k$, recall figure 2.3). Integrating the phase around a Dirac point, where the spin orientation is fully revolving, gives rise to a Berry phase of π [16] and has important consequences for weak antilocalization effects and elastic backscattering in this material [24]; this can be seen from the spin texture. When a charge carrier with momentum k has to elastically scatter into a state with opposite momentum $-k$ then the spin should invert correspondingly which is generally not the case for such scattering events. The scattering probability scales with $(1 + \cos\theta)$ where θ denotes the scattering angle, yielding a finite scattering probability away from 180° scattering, but the reduced backscattering will still enhance the mobility [25].

Instead of looking into the odd or even number of crossings between Kramers pairs, the topological invariant ν_0 can be determined by looking at the parity of the occupied

---

[6]A clear summary on the theoretical and experimental work on topological states in HgTe quantum wells is given in [17].

bands at the time-reversal invariant momenta. This method is only valid when the crystal has inversion symmetry [16] and is related to a vanishing Berry curvature thereby simplifying the calculation of the invariant[7]. As discussed in section 2.1, it can be seen that the crystal structure of $(V)_2(VI)_3$ has indeed inversion symmetry which simplifies the topological classification of this group of materials. In three dimensions, four nonequivalent time-reversal-invariant momenta Γ_i are present in the Brillouin zone [4]. The Z_2 invariant ν_0 at these points can now be calculated by introducing the following quantity δ_i [16]:

$$\delta_i = \prod_{m=1}^{N} \xi_{2m}\left(\Gamma_i\right), \tag{2.4}$$

where $\xi_{2m}\left(\Gamma_i\right) = \pm 1$ is the parity eigenvalue of the $2m^{\text{th}}$ occupied band at time-reversal-invariant momentum point Γ_i. Here, $\xi_{2m} = \xi_{2m-1}$ which comes from the Kramers' degeneracy at the special points. If now the δ_i's are multiplied for all time-reversal-invariant momenta Γ_i, the Z_2 invariant ν_0 is obtained:

$$(-1)^{\nu_0} = \prod_{i} \delta_i. \tag{2.5}$$

Since parity eigenvalues for band structures are well known, it is easy to determine the Z_2 topological class for crystals with inversion symmetry. In the work by Zhang et al., this method has been employed on the $(V)_2(VI)_3$ materials, where it has been determined that Bi_2Se_3, Bi_2Te_3, and Sb_2Te_3 are topological insulators due to the inversion of the bands (with p orbital character) close to the Fermi level by strong spin–orbit coupling [1], similar as that observed for HgTe quantum wells. For Sb_2Se_3, the spin–orbit coupling is not strong enough to facilitate such a band inversion[8]. The change in the overall parity of the occupied bands leads to a topologically nontrivial material with $\nu_0 = 1$. When this material is in connection with a trivial insulator ($\nu_0 = 0$), $\Delta\nu_0 = 1$ yields one Kramers pair of surface states, known as the bulk–boundary correspondence.

One has to realize that such states exist at both top and bottom surfaces. The presence of such a pair will lead to a single chiral edge state at the side surface with a Hall conductance of e^2/h when the system is subject to a large magnetic field. This edge state is shared between the two half-filled Landau levels running oppositely at both surfaces (since the magnetic field is opposite with respect to the surface normal at both surfaces). As shortly touched upon before, the quantum anomalous Hall effect can be realized upon introducing ferromagnetism in the 3D topological insulator, which breaks time-reversal symmetry and opens up a gap that has an opposite sign at top and bottom surface. The different character of the bands at both surfaces requires again a crossover state at the boundary between top and bottom surface that leads to a maximum conductance of e^2/h again. Another important consequence of

---

[7]In a system where both inversion symmetry and time-reversal symmetry are present both $\boldsymbol{V}_n(\boldsymbol{k}) = \boldsymbol{V}_n(-\boldsymbol{k})$ and $\boldsymbol{V}_n(-\boldsymbol{k}) = -\boldsymbol{V}_n(\boldsymbol{k})$ should hold which is only valid if $\boldsymbol{V}_n(\boldsymbol{k}) = 0$. This makes that the Bloch states are also parity eigenstates [1,4].

[8]A feeling for as to why Sb_2Se_3 is a topologically trivial material can be realized from comparing the spin–orbit coupling constants of the separate elements [26].

considering both top and bottom surface is that of size effects where at thicknesses lower than ∼6 nm the surface states can hybridize [27–29]. Such finite-size effects are more easily observable in the HgTe quantum well systems where the critical thickness is on the order of several hundreds of nm [30, 31].

2.3   Bi-based topological insulators

The first experimentally realized 3D topological insulator is $Bi_{1-x}Sb_x$. Upon substitution of Sb into Bi, the lowest unoccupied conduction band and highest occupied valence band invert and yield a gapped structure that is topologically nontrivial. At higher concentrations of Sb, the system turns into a semimetal as it is the case for pristine Bi, but with a nontrivial character in contrast to pure Bi. Using surface-sensitive techniques such as angular-resolved photoemission spectroscopy (ARPES) and scanning tunneling microscopy (STM) the surface states of this 3D topological insulator have been shown. From ARPES experiments [32–34], it has been observed that the surface state shows an odd number of crossings with the Fermi level and that the spin orientation of each state rotates 360° around the Fermi surface (giving a π Berry phase); both clear indicators for the topological nature of these states. Furthermore, the topological character of Sb has been shown [33], but due to its semimetallic character it will be difficult to solely access the topological surface states in transport measurements. From STM measurements [35], the protection against backscattering of charge carriers in the topological surface states has been observed. However, the small band gap and the complicated surface state structure found for this compound limit room-temperature applications since the bulk will contribute to the charge transport in this material easily and masking of the surface states will occur. Nevertheless, the bulk and surface states can be disentangled from quantum oscillations [36].

Other 3D topological insulators were experimentally realized soon after: Bi_2Se_3 [37, 38], Bi_2Te_3 [39–41], and Sb_2Te_3 [41], showing a much simpler band structure compared to $Bi_{1-x}Sb_x$. The band structures are characterized by an indirect bulk band gap of 0.11–0.3 eV at the Γ point where the topological surface is crossing that gap, see figure 2.5. Having the Dirac point inside the band gap, Bi_2Se_3 (gap ∼0.3 eV) is the most suitable material for studying the topologically protected states at room temperature, whereas the Dirac points for Sb_2Te_3 and Bi_2Te_3 lie close to or in the valence band and are thus difficult to access separately from the bulk. Furthermore, it has been found that Bi_2Te_3 suffers from hexagonal warping effects related to spin–orbit coupling that yield out-of-plane spin orientations and thus an increased backscattering [40, 42, 43]. Another advantage over $Bi_{1-x}Sb_x$ is that these materials are stoichiometric crystals and not alloys as is $Bi_{1-x}Sb_x$, which in principle should allow higher purity and a larger homogeneity of the material [4]. However, it turns out that the canonical compound Bi_2Se_3, besides environmental effects (see references in section 3.1), often suffers from Se vacancies that act as electron donors to the system [44–47]. Additionally, antisite defects [48], i.e. atoms exchanging position in the crystal lattice, seem to play a role [47, 49] and contribute to the n-type character [45, 46]. Growing in Bi-rich or Se-rich conditions can lead to lower charge-carrier
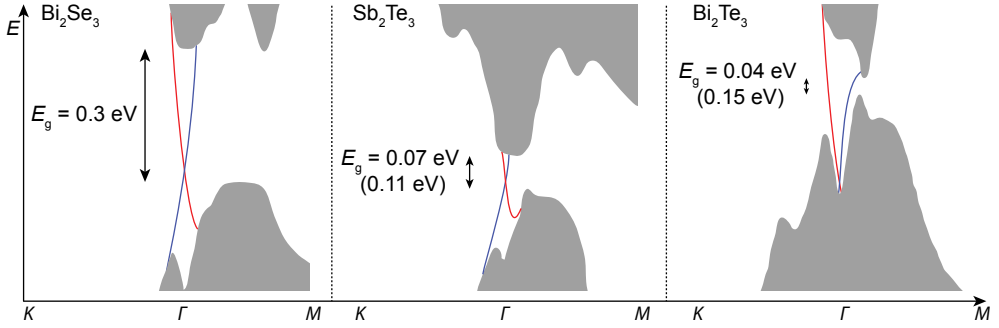
Figure 2.5: Band structures for Bi_2Se_3, Sb_2Te_3, and Bi_2Te_3 through different momentum points as adapted from [1]. The quoted values of the indirect band gap E_g are extracted from calculations [1], whereas the values in brackets indicate the actual band gaps observed in experiments [40, 41].

densities [50, 51], but will always lead to n-type Bi_2Se_3 where the Fermi level is usually located in the bulk conduction band, yielding an intermixing of bulk and surface states in non-surface-sensitive (transport) investigations (see chapter 5)[9]. Substitution of Bi with Sb yields a reduction of defects (lowering the charge-carrier density) [52], while preserving the relatively high mobility. p-type Bi_2Se_3 can be obtained by Ca substitution of Bi [38, 49, 53], but introduction of Ca increases the scattering at the same time and thus lowers the mobility (below 300 cm^2/Vs [53]). An alternative is to use Cd substitution, which preserves the mobilities but is very sensitive to the annealing conditions [54].

As a solution, intermixing of Bi_2Se_3, Sb_2Te_3, and Bi_2Te_3 can yield systems with a balanced charge-carrier density where the different types of defects compete and additional antisite effects can occur [45]. This does not only tune the Fermi level but also the band structure which is a combination of those of the binary compounds [55]. This gives rise to compounds including (Sn-doped) Bi_2Te_2Se [45, 56–62][10], $Bi_2Te_{2.5}Se_{0.5}$ [45], Sb_2Te_2Se [56], $(Bi_{1-x}Sb_x)_2Te_3$ [63–66][11], and $Bi_{2-x}Sb_xTe_{3-y}Se_y$ [55, 59, 67–70]. The mobilities found in these systems are usually not that high, but due to a reduced bulk contribution the surface states take a main role in the transport with the cost of a relatively high resistivity.

2.4   Growth

Depending on the purpose one can apply different techniques for growing topological insulators of which an overview will be given in this section. For this thesis, Bi_2Se_3 films have been mainly grown by molecular-beam epitaxy (MBE) by our collaborators from Rutgers University [71], which will be the main focus of this section. In the second part, other promising growth techniques to unravel the novel properties of

---

[9]Bi_2Te_3 can change from n type to p type by changing the growth conditions [45, 47].

[10]An impurity band seems present that can change the charge-carrier type at lower temperatures.

[11]The insulating compounds show a strong hexagonal warping effect as observed for Bi_2Te_3.

topological insulators are briefly discussed.

2.4.1 Thin films

Large-area thin films of chalcogenide-based topological insulators (containing S, Se, Te; including the alloys $(Bi_{1-x}Sb_x)_2Te_3$ [63] and Bi_2Te_2Se [72]) are usually grown by MBE. MBE is a physical vapor deposition (PVD) technique where the separate elements are (thermally) co-evaporated from Knudsen cells. This separate evaporation, rather than depositing from a single-composite target, yields a good control over the stoichiometry and the growth rates of the layers, by tuning the temperature of the respective cells, thereby tuning the vapor pressure of every element [71][12]. Furthermore, the thermal type of evaporation yields low-energy particles (in contrast to for example electron-beam evaporation) that can easier adsorb on the substrate. Another advantage of MBE over other PVD techniques is that the quality of the grown layer does not depend on the target material but can be controlled by the fluxes from high-purity (>99.999% [71]) element sources.

As already introduced in section 2.1, the topological insulators under consideration consist of layers that have intralayer (in-plane) covalent bonding and interlayer (out-of-plane) Van der Waals bonding. The growth of such materials (called Van der Waals epitaxy) necessitates substrates that are chemically compatible rather than lattice matched, because the interaction with the substrate will be weak [76]. The Bi_2Se_3 samples that we have used in this thesis are obtained from the group of Seongshik Oh at Rutgers University. At Rutgers University, Si(111), Al_2O_3 (0001), amorphous SiO_2, and cubic $SrTiO_3$ (001) substrates have been used to grow Bi_2Se_3, which will be discussed so as to get an understanding of the growth mechanisms of these materials and how this can be related to their charge-transport properties.

Our collaborators started out with growing Bi_2Se_3 on Si(111) because of the relatively good lattice mismatch of +7%. These substrates were passivated by a monolayer of Se that was grown at low temperatures [77]. Subsequently, 3 QL of Bi_2Se_3 were grown as a seed layer at the same temperature, whereafter the temperature was raised to increase the surface mobility of the atoms and thus improve Bi_2Se_3 growth. Triangular features have been observed in the resulting films, which are the structures with the lowest surface free energy and indicators of the high-quality growth. This implies that some order of lattice matching is desired. Upon finding substrates with a lower lattice mismatch than Si(111), In terminated InP(111) (–0.2%) seems to be a good candidate. Using these substrates, a considerable lowering of the charge carrier density (defect density) has been observed relative to samples grown on Si(111) [78].

Growth of Bi_2Se_3 on Al_2O_3(0001) having a larger mismatch of –14% has several advantages: the substrate is much more chemically stable, is able to better withstand higher temperatures (without having any reactions with the grown material), and is insulating. However, one cannot directly grow at higher temperatures, because of the poor sticking coefficient of Bi and Se to the substrate at such high temperatures. Therefore, one has to adopt a two-temperature process as described for the Si(111) substrates. It has been observed that triangular features appear that are much larger

---

[12]The high vapor pressure of Se under moderate temperatures makes a Se capping layer a good candidate to preserve the top surface [73–75].

in feature size [79]. This indicates the high quality of these films and can be related to the lower density of nucleation sites due to the inertness of Al_2O_3. Furthermore, grain boundaries have been observed in the first QL but such defects are not continued in the subsequent layer because of the Van der Waals-type growth of these class of materials. However, these interfacial defects have been found to introduce a significant amount of charge carriers and pin the mobility due to the induced disorder [80]. The disorder is especially apparent in transport measurements on films with thicknesses below 100 nm. The influence of the interfacial defects is smaller for Si(111), which is linked to a higher bulk-defect density dominating the charge-transport properties, but casts doubts on the origin of the thickness-independent transport channels, as reported earlier [79, 80]. Furthermore, it has been observed that Se diffusion through the material can play an important role in the thickness-dependent charge-transport properties [81].

For that reason, In_2Se_3 (having a lattice mismatch of –3.3% with Bi_2Se_3) was introduced as a buffer layer on top of the 3 QL Bi_2Se_3 seed layer to separate the interfacial defects from the transport channel. In order to obtain an insulating behavior, annealing followed the In_2Se_3 buffer layer deposition which leads to intermixing of seed and buffer layer where $(Bi_{1-x}In_x)_2Se_3$ is insulating (and topologically trivial) when $x > 30$ [82]. However, on top of the buffer layer (still In_2Se_3) Bi_2Se_3 could not be directly grown due to intermixing of In and Bi [83], which will lead to another insulating phase [82]. Therefore, another layer of $(Bi_{0.5}In_{0.5})_2Se_3$ was grown where one can imagine that the Bi binds to the In such that intermixing is prevented. This has led to Bi_2Se_3 layers with a record-high mobility of 15,000 cm^2/Vs and observation of the quantum Hall effect [84][13], where in the end the interfacial defect density still dominates at smaller thicknesses.

Using amorphous SiO_2 or cubic $SrTiO_3$ [87] as substrate still yields a 2D growth but because of a missing hexagonal crystalline phase at the substrate's surface, the layers are randomly oriented while preserving growth along the c axis (showing twinning). One example of growth on SiO_2 has been reported by Bansal et al. [88], where it has been observed that SiO_2 seems to outperform Si(111), related to the chemical reactivity of the Si(111) samples. Other substrates that have been used (outside the work by Rutgers) are graphene-terminated SiC(0001) [28, 89] (being conducting), GaAs(111) [90] (not showing any preferential orientation of growth), and the promising CdS(0001) with a reasonably high charge-carrier mobility [91].

Another PVD technique that has been employed is pulsed laser deposition (PLD) where a material from a target is laser ablated. The reports on PLD-grown topological insulators are limited, but the grown films often show a very low mobility (on the order of 10 cm^2/Vs) [92–94]. Magnetron-sputtered Bi_2Se_3 shows a very large charge-carrier density [95], yielding strong intermixing of bulk states.

---

[13]The quantum Hall effect was observed earlier for $Bi_{2-x}Sb_xTe_{3-y}Se_y$ [85] and $(Bi_{1-x}Sb_x)_2Te_3$ [86], relying on a tuning of the charge carrier density closer to the Dirac point rather than improvement of mobility.

2.4.2 Bulk crystals, nanoplatelets, and nanoribbons

Since the discussed topological insulators have a layered crystal structure with a weak Van der Waals-bonding between the layers, such materials can be easily mechanically exfoliated from bulk crystals and be placed on any arbitrary substrate. Bulk single crystals are usually grown by the Bridgman method [96] where the element materials are placed in a sealed quartz-glass tube, heated up to high temperatures (for mixing), and then cooled down to solidify with a temperature gradient along the tube such that the crystal grows at one end of the tube. Tuning the ratios of the elements, one can get the compound $Bi_{2-x}Sb_xTe_{3-y}Se_y$ for any x and y. Since this is a rather straightforward technique and widely used in the community (and found in many papers cited in this thesis), I will not further discuss this method here. Another technique that has been used to obtain bulk crystals is chemical-vapor transport (CVT) where gases containing the elements of interest, usually together with an I_2 transport gas, are forming such crystals [97].

The method of CVT can also yield growth of nanoplatelets and nanoribbons which are interesting because of their finite-size effects and enhanced surface-to-bulk ratio. Such structures can be grown on an arbitrary substrate, either with or without catalyst at the substrate [98–104]; sometimes with rather high mobilities [101]. Such nanoplatelets can nucleate to form a larger network of topological insulator material. However, the platelet growth initiates from random nucleation sites and this therefore leads to a random orientation of the films. Without any chemical reaction, it has been shown that Bi_2Se_3 nanoribbons can be formed by a catalyst-free PVD technique too where gaseous Bi_2Se_3 yields growth on a substrate [105]. The growth techniques described here are usually easy (no high-vacuum systems) and easy to employ. As with the mechanical cleavage of crystals, the shape, size, and position of the nanostructures is undetermined beforehand, due to the sensitive growth parameters, and are therefore more employed in an academic setting rather than (yet) being very suitable for industrial implementation.

2.5 References

[1] H. Zhang, et al., "Topological insulators in Bi_2Se_3, Bi_2Te_3 and Sb_2Te_3 with a single Dirac cone on the surface," *Nature Physics* **5**, pp. 438–442, June 2009.

[2] W. Zhang, et al., "First-principles studies of the three-dimensional strong topological insulators Bi_2Te_3, Bi_2Se_3 and Sb_2Te_3," *New Journal of Physics* **12**, p. 065013, June 2010.

[3] X. Chen, et al., "Thermal expansion coefficients of Bi_2Se_3 and Sb_2Te_3 crystals from 10 K to 270 K," *Applied Physics Letters* **99**, p. 261912, Dec. 2011.

[4] M. Z. Hasan and C. L. Kane, "Colloquium: Topological insulators," *Reviews of Modern Physics* **82**, pp. 3045–3067, Nov. 2010.

[5] A. Akhmerov, et al., "Topology in Condensed Matter: Tying Quantum Knots," July 2017. https://topocondmat.org/.

[6] K. v. Klitzing, et al., "New Method for High-Accuracy Determination of the Fine-Structure Constant Based on Quantized Hall Resistance," *Physical Review Letters* **45**, pp. 494–497, Aug. 1980.

[7] B. I. Halperin, "Quantized Hall conductance, current-carrying edge states, and the existence of extended states in a two-dimensional disordered potential," *Physical Review B* **25**, pp. 2185–2190, Feb. 1982.

[8] D. J. Thouless, et al., "Quantized Hall Conductance in a Two-Dimensional Periodic Potential," *Physical Review Letters* **49**, pp. 405–408, Aug. 1982.

[9] M. V. Berry, "Quantal Phase Factors Accompanying Adiabatic Changes," *Proceedings of the Royal Society of London. A. Mathematical and Physical Sciences* **392**, pp. 45–57, Mar. 1984.

[10] F. D. M. Haldane, "Model for a Quantum Hall Effect without Landau Levels: Condensed-Matter Realization of the "Parity Anomaly"," *Physical Review Letters* **61**, pp. 2015–2018, Oct. 1988.

References

[11] C.-Z. Chang, et al., "Experimental Observation of the Quantum Anomalous Hall Effect in a Magnetic Topological Insulator," *Science* **340**, pp. 167–170, Apr. 2013.

[12] C.-Z. Chang, et al., "High-precision realization of robust quantum anomalous Hall state in a hard ferromagnetic topological insulator," *Nature Materials* **14**, pp. 473–477, May 2015.

[13] C. L. Kane and E. J. Mele, "Quantum Spin Hall Effect in Graphene," *Physical Review Letters* **95**, p. 226801, Nov. 2005.

[14] C. L. Kane and E. J. Mele, "Z_2 Topological Order and the Quantum Spin Hall Effect," *Physical Review Letters* **95**, p. 146802, Sept. 2005.

[15] J. E. Moore and L. Balents, "Topological invariants of time-reversal-invariant band structures," *Physical Review B* **75**, p. 121306, Mar. 2007.

[16] L. Fu and C. L. Kane, "Topological insulators with inversion symmetry," *Physical Review B* **76**, p. 045302, July 2007.

[17] M. König, et al., "The Quantum Spin Hall Effect: Theory and Experiment," *Journal of the Physical Society of Japan* **77**, p. 031007, Mar. 2008.

[18] H. Min, et al., "Intrinsic and Rashba spin-orbit interactions in graphene sheets," *Physical Review B* **74**, p. 165310, Oct. 2006.

[19] Y. Yao, et al., "Spin-orbit gap of graphene: First-principles calculations," *Physical Review B* **75**, p. 041401, Jan. 2007.

[20] B. A. Bernevig, et al., "Quantum Spin Hall Effect and Topological Phase Transition in HgTe Quantum Wells," *Science* **314**, pp. 1757–1761, Dec. 2006.

[21] M. König, et al., "Quantum Spin Hall Insulator State in HgTe Quantum Wells," *Science* **318**, pp. 766–770, Nov. 2007.

[22] A. Roth, et al., "Nonlocal Transport in the Quantum Spin Hall State," *Science* **325**, pp. 294–297, July 2009.

[23] C. Brüne, et al., "Spin polarization of the quantum spin Hall edge states," *Nature Physics* **8**, pp. 485–490, June 2012.

[24] T. Ando, et al., "Berry's Phase and Absence of Back Scattering in Carbon Nanotubes," *Journal of the Physical Society of Japan* **67**, pp. 2857–2862, Aug. 1998.

[25] D. Culcer, et al., "Two-dimensional surface charge transport in topological insulators," *Physical Review B* **82**, p. 155457, Oct. 2010.

[26] K. Wittel and R. Manne, "Atomic spin-orbit interaction parameters from spectral data for 19 elements," *Theoretica chimica acta* **33**, pp. 347–349, Dec. 1974.

[27] J. Linder, et al., "Anomalous finite size effects on surface states in the topological insulator Bi_2Se_3," *Physical Review B* **80**, p. 205401, Nov. 2009.

[28] Y. Zhang, et al., "Crossover of the three-dimensional topological insulator Bi_2Se_3 to the two-dimensional limit," *Nature Physics* **6**, pp. 584–588, Aug. 2010.

[29] A. A. Taskin, et al., "Manifestation of Topological Protection in Transport Properties of Epitaxial Bi_2Se_3 Thin Films," *Physical Review Letters* **109**, p. 066803, Aug. 2012.

[30] B. Zhou, et al., "Finite Size Effects on Helical Edge States in a Quantum Spin-Hall System," *Physical Review Letters* **101**, p. 246807, Dec. 2008.

[31] C. Brüne, et al., "Evidence for the ballistic intrinsic spin Hall effect in HgTe nanostructures," *Nature Physics* **6**, pp. 448–454, June 2010.

[32] D. Hsieh, et al., "A topological Dirac insulator in a quantum spin Hall phase," *Nature* **452**, pp. 970–974, Apr. 2008.

[33] D. Hsieh, et al., "Observation of Unconventional Quantum Spin Textures in Topological Insulators," *Science* **323**, pp. 919–922, Feb. 2009.

[34] A. Nishide, et al., "Direct mapping of the spin-filtered surface bands of a three-dimensional quantum spin Hall insulator," *Physical Review B* **81**, p. 041309, Jan. 2010.

[35] P. Roushan, et al., "Topological surface states protected from backscattering by chiral spin texture," *Nature* **460**, pp. 1106–1109, Aug. 2009.

[36] A. A. Taskin and Y. Ando, "Quantum oscillations in a topological insulator $Bi_{1-x}Sb_x$," *Physical Review B* **80**, p. 085303, Aug. 2009.

[37] Y. Xia, et al., "Observation of a large-gap topological-insulator class with a single Dirac cone on the surface," *Nature Physics* **5**, pp. 398–402, June 2009.

[38] D. Hsieh, et al., "A tunable topological insulator in the spin helical Dirac transport regime," *Nature* **460**, pp. 1101–1105, Aug. 2009.

[39] H.-J. Noh, et al., "Spin-orbit interaction effect in the electronic structure of Bi_2Te_3 observed by angle-resolved photoemission spectroscopy," *Europhysics Letters* **81**(5), p. 57006, 2008.

[40] Y. L. Chen, et al., "Experimental Realization of a Three-Dimensional Topological Insulator, Bi_2Te_3," *Science* **325**, pp. 178–181, July 2009.

[41] D. Hsieh, et al., "Observation of Time-Reversal-Protected Single-Dirac-Cone Topological-Insulator States in Bi_2Te_3 and Sb_2Te_3," *Physical Review Letters* **103**, p. 146401, Sept. 2009.

[42] Z. Alpichshev, et al., "STM Imaging of Electronic Waves on the Surface of Bi_2Te_3: Topologically Protected Surface States and Hexagonal Warping Effects," *Physical Review Letters* **104**, p. 016401, Jan. 2010.

[43] S. Souma, et al., "Direct Measurement of the Out-of-Plane Spin Texture in the Dirac-Cone Surface State of a Topological Insulator," *Physical Review Letters* **106**, p. 216803, May 2011.

[44] J. Navrátil, et al., "Conduction band splitting and transport properties of Bi_2Se_3," *Journal of Solid State Chemistry* **177**, pp. 1704–1712, Apr. 2004.

[45] D. O. Scanlon, et al., "Controlling Bulk Conductivity in Topological Insulators: Key Role of AntiSite Defects," *Advanced Materials* **24**, pp. 2154–2158, Apr. 2012.

[46] D. West, et al., "Native defects in second-generation topological insulators: Effect of spin-orbit interaction on Bi_2Se_3," *Physical Review B* **86**, p. 121201, Sept. 2012.

[47] L.-L. Wang, et al., "Native defects in tetradymite $Bi_2(Te_xSe_{3-x})$ topological insulators," *Physical Review B* **87**, p. 125303, Mar. 2013.

[48] J. Horák, et al., "Anti-site defects in n-Bi_2Se_3 crystals," *Journal of Physics and Chemistry of Solids* **51**, pp. 1353–1360, Jan. 1990.

[49] Y. S. Hor, et al., "p-type Bi_2Se_3 for topological insulator and low-temperature thermoelectric applications," *Physical Review B* **79**, p. 195208, May 2009.

[50] N. P. Butch, et al., "Strong surface scattering in ultrahigh-mobility Bi_2Se_3 topological insulator crystals," *Physical Review B* **81**, p. 241301, June 2010.

[51] J. G. Analytis, et al., "Bulk Fermi surface coexistence with Dirac surface state in Bi_2Se_3: A comparison of photoemission and Shubnikov-de Haas measurements," *Physical Review B* **81**, p. 205407, May 2010.

[52] J. G. Analytis, et al., "Two-dimensional surface state in the quantum limit of a topological insulator," *Nature Physics* **6**, pp. 960–964, Dec. 2010.

[53] J. G. Checkelsky, et al., "Quantum Interference in Macroscopic Crystals of Nonmetallic Bi_2Se_3," *Physical Review Letters* **103**, p. 246601, Dec. 2009.

[54] Z. Ren, et al., "Observations of two-dimensional quantum oscillations and ambipolar transport in the topological insulator Bi_2Se_3 achieved by Cd doping," *Physical Review B* **84**, p. 075316, Aug. 2011.

[55] T. Arakane, et al., "Tunable Dirac cone in the topological insulator $Bi_{2-x}Sb_xTe_{3-y}Se_y$," *Nature Communications* **3**, p. 636, Jan. 2012.

[56] S.-Y. Xu, et al., "Discovery of several large families of Topological Insulator classes with backscattering-suppressed spin-polarized single-Dirac-cone on the surface," *arXiv* , p. 1007.5111, July 2010.

[57] Z. Ren, et al., "Large bulk resistivity and surface quantum oscillations in the topological insulator Bi_2Te_2Se," *Physical Review B* **82**, p. 241306, Dec. 2010.

[58] S. Jia, et al., "Low-carrier-concentration crystals of the topological insulator Bi_2Te_2Se," *Physical Review B* **84**, p. 235206, Dec. 2011.

[59] Z. Ren, et al., "Optimizing $Bi_{2-x}Sb_xTe_{3-y}Se_y$ solid solutions to approach the intrinsic topological insulator regime," *Physical Review B* **84**, p. 165311, Oct. 2011.

[60] S. Jia, et al., "Defects and high bulk resistivities in the Bi-rich tetradymite topological insulator $Bi_{2+x}Te_{2-x}Se$," *Physical Review B* **86**, p. 165119, Oct. 2012.

[61] Z. Ren, et al., "Fermi level tuning and a large activation gap achieved in the topological insulator Bi_2Te_2Se by Sn doping," *Physical Review B* **85**, p. 155301, Apr. 2012.

[62] J. Xiong, et al., "Quantum oscillations in a topological insulator Bi_2Te_2Se with large bulk resistivity (6 Ω cm)," *Physica E: Low-dimensional Systems and Nanostructures* **44**, pp. 917–920, Feb. 2012.

[63] J. Zhang, et al., "Band structure engineering in $(Bi_{1-x}Sb_x)_2Te_3$ ternary topological insulators," *Nature Communications* **2**, p. 1588, Dec. 2011.

[64] D. Kong, et al., "Ambipolar field effect in the ternary topological insulator $(Bi_{1-x}Sb_x)_2Te_3$ by composition tuning," *Nature Nanotechnology* **6**, pp. 705–709, Nov. 2011.

[65] X. He, et al., "Highly tunable electron transport in epitaxial topological insulator $(Bi_{1-x}Sb_x)_2Te_3$ thin films," *Applied Physics Letters* **101**, p. 123111, Sept. 2012.

[66] C. Weyrich, et al., "Growth, characterization, and transport properties of ternary $(Bi_{1-x}Sb_x)_2Te_3$ topological insulator layers," *Journal of Physics: Condensed Matter* **28**(49), p. 495501, 2016.

[67] A. A. Taskin, et al., "Observation of Dirac Holes and Electrons in a Topological Insulator," *Physical Review Letters* **107**, p. 016801, June 2011.

[68] K. Segawa, et al., "Ambipolar transport in bulk crystals of a topological insulator by gating with ionic liquid," *Physical Review B* **86**, p. 075306, Aug. 2012.

[69] Y. Pan, et al., "Low carrier concentration crystals of the topological insulator $Bi_{2-x}Sb_xTe_{3-y}Se_y$: a magnetotransport study," *New Journal of Physics* **16**, p. 123035, Dec. 2014.

[70] Y. Pan, et al., "Quantum oscillations of the topological surface states in low carrier concentration crystals of $Bi_{2-x}Sb_xTe_{3-y}Se_y$," *Solid State Communications* **227**, pp. 13–18, Feb. 2016.

[71] M. J. Brahlek, *Atomic scale engineering of topological materials.* PhD thesis, Rutgers, the State University of New Jersey, New Brunswick, New Jersey, Oct. 2014.

[72] Y. Tung, et al., "Growth and characterization of molecular beam epitaxy-grown $Bi_2Te_{3-x}Se_x$ topological insulator alloys," *Journal of Applied Physics* **119**, p. 055303, Feb. 2016.

[73] K. Virwani, et al., "Controlled removal of amorphous Se capping layer from a topological insulator," *Applied Physics Letters* **105**, p. 241605, Dec. 2014.

[74] J. Dai, et al., "Restoring pristine Bi_2Se_3 surfaces with an effective Se decapping process," *Nano Research* **8**, pp. 1222–1228, Apr. 2015.

[75] M. Salehi, et al., "Stability of low-carrier-density topological-insulator Bi_2Se_3 thin films and effect of capping layers," *APL Materials* **3**, p. 091101, Sept. 2015.

[76] A. Koma, "Van der Waals epitaxy — a new epitaxial growth method for a highly lattice-mismatched system," *Thin Solid Films* **216**, pp. 72–76, Aug. 1992.

[77] N. Bansal, et al., "Epitaxial growth of topological insulator Bi_2Se_3 film on Si(111) with atomically sharp interface," *Thin Solid Films* **520**, pp. 224–229, Oct. 2011.

References

[78] X. Guo, et al., "Single domain Bi_2Se_3 films grown on InP(111)A by molecular-beam epitaxy," *Applied Physics Letters* **102**, p. 151604, Apr. 2013.

[79] N. Bansal, et al., "Thickness-Independent Transport Channels in Topological Insulator Bi_2Se_3 Thin Films," *Physical Review Letters* **109**, p. 116804, Sept. 2012.

[80] J. Hellerstedt, et al., "Thickness and growth-condition dependence of in-situ mobility and carrier density of epitaxial thin-film Bi_2Se_3," *Applied Physics Letters* **105**, p. 173506, Oct. 2014.

[81] Y. S. Kim, et al., "Thickness-dependent bulk properties and weak antilocalization effect in topological insulator Bi_2Se_3," *Physical Review B* **84**, p. 073109, Aug. 2011.

[82] M. Brahlek, et al., "Topological-Metal to Band-Insulator Transition in $(Bi_{1-x}In_x)_2Se_3$ Thin Films," *Physical Review Letters* **109**, p. 186403, Oct. 2012.

[83] H. D. Lee, et al., "Indium and bismuth interdiffusion and its influence on the mobility in In_2Se_3/Bi_2Se_3," *Thin Solid Films* **556**, pp. 322–324, Apr. 2014.

[84] N. Koirala, et al., "Record Surface State Mobility and Quantum Hall Effect in Topological Insulator Thin Films via Interface Engineering," *Nano Letters* **15**, pp. 8245–8249, Dec. 2015.

[85] Y. Xu, et al., "Observation of topological surface state quantum Hall effect in an intrinsic three-dimensional topological insulator," *Nature Physics* **10**, pp. 956–963, Dec. 2014.

[86] R. Yoshimi, et al., "Quantum Hall effect on top and bottom surface states of topological insulator $(Bi_{1-x}Sb_x)_2Te_3$ films," *Nature Communications* **6**, p. 7627, Apr. 2015.

[87] J. Chen, et al., "Gate-Voltage Control of Chemical Potential and Weak Antilocalization in Bi_2Se_3," *Physical Review Letters* **105**, p. 176602, Oct. 2010.

[88] N. Bansal, et al., "Robust topological surface states of Bi_2Se_3 thin films on amorphous SiO_2/Si substrate and a large ambipolar gating effect," *Applied Physics Letters* **104**, p. 241606, June 2014.

[89] P. Cheng, et al., "Landau Quantization of Topological Surface States in Bi_2Se_3," *Physical Review Letters* **105**, p. 076801, Aug. 2010.

[90] A. Richardella, et al., "Coherent heteroepitaxy of Bi_2Se_3 on GaAs (111)B," *Applied Physics Letters* **97**, p. 262104, Dec. 2010.

[91] X. F. Kou, et al., "Epitaxial growth of high mobility Bi_2Se_3 thin films on CdS," *Applied Physics Letters* **98**, p. 242102, June 2011.

[92] Y. Onose, et al., "Pulsed Laser Deposition and Ionic Liquid Gate Control of Epitaxial Bi_2Se_3 Thin Films," *Applied Physics Express* **4**, p. 083001, July 2011.

[93] L. Meng, et al., "Growth and characterization of Bi_2Se_3 thin films by pulsed laser deposition using alloy target," *Thin Solid Films* **519**, pp. 7627–7631, Sept. 2011.

[94] P. H. Le, et al., "Growth and characterization of topological insulator Bi_2Se_3 thin films on $SrTiO_3$ using pulsed laser deposition," *Thin Solid Films* **534**, pp. 659–665, May 2013.

[95] W. J. Wang, et al., "Thickness-dependent transport channels in topological insulator Bi_2Se_3 thin films grown by magnetron sputtering," *Scientific Reports* **6**, p. 25291, May 2016.

[96] P. W. Bridgman, "Certain physical properties of single crystals of tungsten, antimony, bismuth, tellurium, cadmium, zinc, and tin," *Proceedings of the American Academy of Arts and Sciences* **60**(6), pp. 305–383, 1925.

[97] W. H. Jiao, et al., "Growth and characterization of Bi_2Se_3 crystals by chemical vapor transport," *AIP Advances* **2**, p. 022148, June 2012.

[98] D. Kong, et al., "Few-Layer Nanoplates of Bi_2Se_3 and Bi_2Te_3 with Highly Tunable Chemical Potential," *Nano Letters* **10**, pp. 2245–2250, June 2010.

[99] H. Peng, et al., "Aharonov-Bohm interference in topological insulator nanoribbons," *Nature Materials* **9**, pp. 225–229, Mar. 2010.

[100] W. Dang, et al., "Epitaxial Heterostructures of Ultrathin Topological Insulator Nanoplate and Graphene," *Nano Letters* **10**, pp. 2870–2876, Aug. 2010.

[101] P. Gehring, et al., "Growth of High-Mobility Bi_2Te_2Se Nanoplatelets on hBN Sheets by van der Waals Epitaxy," *Nano Letters* **12**, pp. 5137–5142, Oct. 2012.

[102] R. B. Jacobs-Gedrim, et al., "Chemical assembly and electrical characteristics of surface-rich topological insulator Bi_2Se_3 nanoplates and nanoribbons," *Applied Physics Letters* **101**, p. 143103, Oct. 2012.

[103] J. T. Mlack, et al., "Substrate-independent catalyst-free synthesis of high-purity Bi_2Se_3 nanostructures," *Applied Physics Letters* **102**, p. 193108, May 2013.

[104] C. Nowka, et al., "Catalyst-free Growth of Single Crystalline Bi_2Se_3 Nanostructures for Quantum Transport Studies," *Crystal Growth & Design* **15**, pp. 4272–4278, Sept. 2015.

[105] L. Fang, et al., "Catalyst-Free Growth of Millimeter-Long Topological Insulator Bi_2Se_3 Nanoribbons and the Observation of the π-Berry Phase," *Nano Letters* **12**, pp. 6164–6169, Dec. 2012.